

## Combined acoustic relocation and acoustophoretic migration for particle transfer between co-flowing fluids in a microchannel

A. Nath,<sup>1</sup> L. Malik,<sup>1</sup> and A. K. Sen<sup>1,2,\*</sup>

<sup>1</sup>*Fluid Systems Laboratory, Department of Mechanical Engineering, Indian Institute of Technology Madras, Chennai - 600036, Tamilnadu, India*

<sup>2</sup>*Micro Nano Bio-Fluidics Group, Indian Institute of Technology Madras, Chennai - 600036, Tamilnadu, India*



(Received 17 September 2020; accepted 23 March 2021; published 7 April 2021)

Inhomogeneous co-flowing fluids inside a microchannel exposed to an acoustic standing wave can lead to the relocation of the fluids. Here we investigate the use of combined acoustic relocation and acoustophoretic migration for the transfer of particles between co-flowing fluids inside a microchannel exposed to a standing pressure half-wave with a pressure nodal plane along the channel center line and antinodal planes along the walls. We show that under the influence of the applied field, particles suspended in a carrier fluid of low acoustic impedance flowing along the channel center are initially dragged toward the walls along with the relocating fluid and later migrate into the target fluid that relocates from the walls to the channel center. We found that the particle motion is initially controlled by the dominant fluid relocation-induced Stokes drag force and later governed by the primary acoustic radiation force as stable fluid configuration is reached. Experimentally we unraveled that depending on the operating parameters—particle size, flow rates, and acoustic energy density—the final locations of the particles at the end of the channel leads to three distinct regimes—complete medium exchange, partial medium exchange, and no medium exchange. Our study reveals that the relocation and migration dynamics of the particles is underpinned by the relevant timescales—advection timescale, acoustophoretic timescale, and the relocation timescale, which in turn govern the different regimes observed. Numerical simulations predicted the complete migration and nonmigration of particles of two different sizes, in agreement with the experimental observations. We also demonstrate the medium exchange and size-based sorting of biological cells, which shows the potential application of the study in biochemical assays.

DOI: [10.1103/PhysRevFluids.6.044201](https://doi.org/10.1103/PhysRevFluids.6.044201)

### I. INTRODUCTION

Acoustofluidics involves the use of ultrasonic waves in fluids to achieve different processes such as sorting and separation [1–12], concentration [13,14], trapping and tweezing [15–18] of particles, droplets, and cells, and characterization of the acoustomechanical properties of cells [19,20]. In the presence of a standing acoustic wave, a particle experiences a time-averaged force termed the primary acoustic radiation force, which is proportional to its volume and is dependent on its density and compressibility with respect to that of the suspending fluid [21,22]. Interaction of a particle with waves scattered by other nearby particles introduces an additional force, termed the secondary or interparticle force [23,24], which is generally a few orders of magnitude smaller than the primary

---

\*ashis@iitm.ac.in

force [25]. A detailed exposition of the primary and secondary acoustic radiation forces on a particle exposed to sound waves can be found elsewhere [23,26].

For the flow of a suspension in a microchannel exposed to a standing half-wave orthogonal to the direction of flow, the radiation force drives the suspended solid particles toward the channel center. In a co-flow of fluids of different acoustic properties in a channel having acoustic resonance along the width, for example, a central fluid of relatively lower acoustic impedance flanked by fluid of higher acoustic impedance at the sides, force at the fluid interface can result in bulk transport of entire fluid streams where they relocate with respect to each other, i.e., the fluid flowing initially at the sides is relocated to the nodal region at the channel center while the lower impedance central fluid is relocated to the antinodal region at the walls [27–29]. If the fluid present initially at the sides has relatively lower acoustic impedance, this force tends to stabilize the fluids against gravitational stratification [27]. While in the case of miscible fluids acoustic relocation can occur even for a very small ( $\sim 0.1\%$ ) acoustic impedance contrast, for the case of co-flowing immiscible fluids the acoustic relocation is governed by the competition between acoustic force and interfacial tension force, i.e., the acoustocapillary number [29,30]. If the central fluid (of low impedance) in a co-flow of miscible fluids is a suspension, the suspended particles are also carried along with the relocating fluid to the sides due to Stokes drag force. In the case of suspensions containing particles of different sizes, owing to higher primary acoustic radiation force, the larger-sized particles are driven back to the central pressure node faster compared to smaller particles, and this offers a technique for separation of submicron-sized particles from micron-sized particles [31]. In the case of high-concentration suspensions, the relocation process is more complex as the local properties of the fluid are influenced by the particle volume fraction. This can lead to a partial relocation regime in which a dense suspension initially flowing at the sides splits into two streams where only the denser band relocates to the pressure node [12].

Cell washing, or transfer of cells from a carrier medium to a target medium, is a necessary step for sample preparation in many biomedical applications [32,33]. The traditional technique of medium exchange using acoustic fields involves flowing the carrier medium at the sides and the target medium through the center of the channel [34]. The particles travel from the carrier medium to the target medium under the influence of the primary radiation force. For smaller particles, this acoustophoretic force is relatively smaller, and sufficiently low flow rates need to be employed for complete medium exchange. Also, the presence of particles closer to the walls is performance limiting as the acoustophoretic force is lowest at the walls (antinodes). This latter problem is generally circumvented by introducing a prefocusing stage before the main separation channel [14]. The conventional technique for medium exchange could lead to contamination of the target medium, which is attributed to multiple sources [35]: (a) diffusion of the carrier and target media, which is generally minimized by increasing the flow rates of the media [36]; (b) the effect of acoustic streaming, which can be greatly reduced by having an acoustic impedance mismatch between the target and carrier media which confines the streaming rolls to a very small region close to the walls [37]; (c) the hydrodynamic coupling of particles and the suspending medium at high particle concentrations affects the medium exchange [38]; (d) the effect of flow perturbations, which can be prevented by ensuring a stable flow condition in the channel; and (e) undesirable acoustic relocation of media, which requires that the acoustic impedance of the target medium at the center be higher than the carrier medium at the sides [27].

The medium exchange techniques explored previously have relied on the use of primary acoustic radiation force alone to transfer particles from the relatively low impedance carrier medium at the flowing at the sides to the target medium flowing at the center. The use of acoustic relocation as a technique for exchange of particles between two media has not been studied. More importantly, understanding of the underlying physics of particle motion due to the combined relocation and radiation forces is missing in the literature. Here we propose and investigate a new strategy of medium exchange by introducing the carrier fluid (medium I) of lower acoustic impedance at the center and target fluid of higher acoustic impedance (medium II) at the sides (Fig. 1). On exposure to acoustic standing wave, the medium I relocates to the sides and the target medium (II)

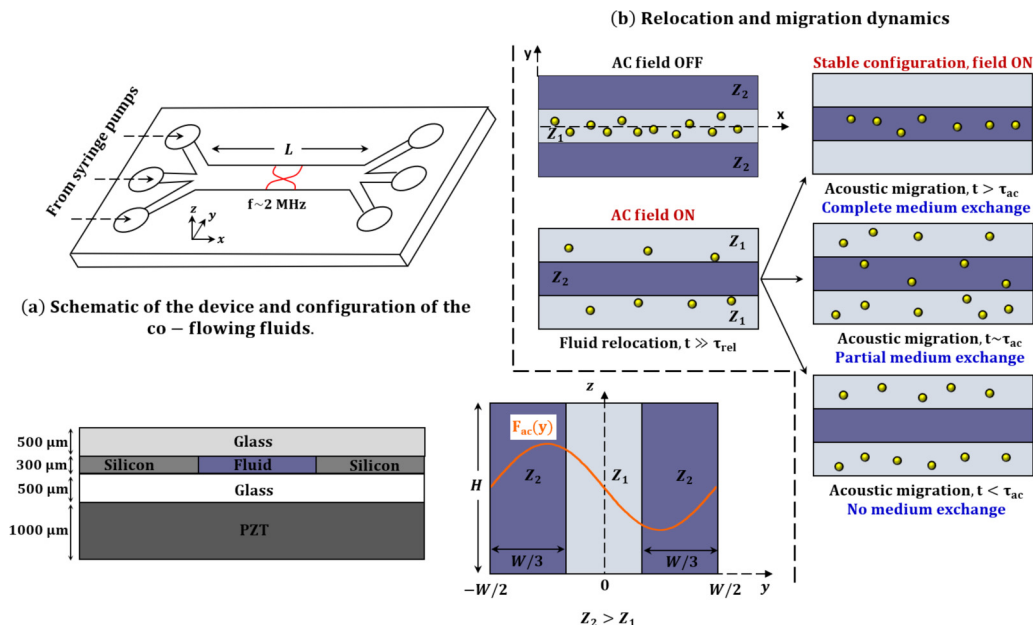


FIG. 1. (a) Schematic representation showing isometric and side views (not to scale) of the acoustofluidic device used in our experiments and the initial configuration of the co-flow with the low acoustic impedance ( $Z_1$ ) fluid at the center and high acoustic impedance ( $Z_2$ ) fluid at the sides. The sinusoidal variation of the primary radiation force  $F_{ac}(y)$  along the channel width is also shown. (b) The final configuration of particles suspended initially in the low impedance central fluid and the final stable configurations under combined effects are shown. After completion of fluid relocation, three possible medium exchange regimes are observed—complete exchange, partial exchange, and no exchange of medium.

relocates to the center. The particles present initially in the central fluid (I) are first dragged along with it toward the walls but later focused toward the center and transferred into the target medium due to the primary acoustic radiation force. We first study experimentally the dynamic behavior of particles under the combined effect of acoustic relocation and migration. We examine the particle dynamics based on the effects of the acoustic relocation-induced drag force and the primary acoustic radiation forces and explain the different regimes (Fig. 1)—complete exchange, partial exchange, and no exchange, in terms of the ratios of the relevant timescales, namely, the acoustic migration timescale, relocation timescale, and residence timescale. A simple numerical model is used to study the medium exchange behavior of particles of two different (10 and 2  $\mu\text{m}$ ) sizes, which shows a good agreement with experimental observations. Finally, we demonstrate the technique for medium exchange of HeLa cells and the separation of HeLa cells from diluted whole blood.

## II. THEORY

In this section we describe the different forces of acoustic origin acting on an inhomogeneous system of fluids containing suspended particles or cells. When an acoustic field is imposed on a suspension, the acoustic wave is scattered by the particles leading to a time-averaged radiation force acting on them. The primary radiation force experienced by a spherical particle in the presence of an acoustic standing wave is well established. For a planar one-dimensional system actuated by a half-wave in the  $y$  direction (i.e., where the width of the channel is half the wavelength  $W = \lambda/2$ , see Fig. 1) the primary radiation force on a spherical particle in the direction of the wave propagation

can be written as [39]

$$\mathbf{F}_{\text{ac}} = 4\pi a^3 \phi(\tilde{\kappa}, \tilde{\rho}) k E_{\text{ac}} \sin(2ky) \mathbf{e}_y, \quad (1)$$

$$\phi = \frac{1 - \tilde{\kappa}}{3} + \frac{2(\tilde{\rho} - 1)}{2\tilde{\rho} + 1}, \quad (2)$$

where  $a$  is the radius of the particle,  $k = \pi/W$  is the wave number,  $\phi(\tilde{\kappa}, \tilde{\rho})$  is the acoustic contrast factor defined in terms of the ratios of the particle to suspending fluid density ( $\tilde{\rho} = \rho_p/\rho_f$ ) and compressibility ( $\tilde{\kappa} = \kappa_p/\kappa_f$ ), and  $E_{\text{ac}}$  is the acoustic energy density in the system. The unit vectors along the  $(x, y, z)$  directions in the coordinate system are represented as  $(\mathbf{e}_x, \mathbf{e}_y, \mathbf{e}_z)$ . The inviscid fluid assumption used in deriving the above expression generally holds as long as the particles are significantly larger than the viscous penetration depth [40]. The expression for radiation force including viscous corrections [26,41] shows that when the suspended particles are near neutrally buoyant (density ratio  $\tilde{\rho} \approx 1$ ), the relative change in the primary radiation force due to the viscous correction term is negligibly small ( $\ll 0.5\%$ ) and hence under the conditions used in this study [Eq. (1)] is adequate. The interparticle secondary radiation force arising from interaction with the scattered acoustic waves is generally a few orders of magnitude smaller than the primary radiation force and is neglected in most cases [25]. The secondary radiation force may however be significant when there are a large number of particles, for example in the case of concentrated suspensions.

Similar to the acoustic radiation force on a suspended particle, the presence of two co-flowing fluids with different properties (density  $\rho_f$ , compressibility  $\kappa_f = 1/\rho_f c_f^2$  where  $c_f$  is the speed of sound in the fluid), leads to a force at the fluid-fluid interface. As explained earlier, this force transports the fluid stream of higher acoustic impedance ( $Z = \rho c$ ) to the pressure node. Therefore, for a fluid configuration with the fluid I of lower acoustic impedance  $Z_{\text{I}}$  initially flowing at the center flanked on either side by fluid II of higher acoustic impedance  $Z_{\text{II}}$ , the interfacial force (or its volume-based implementation, the acoustic force density  $\mathbf{f}_{\text{ac}}$ ) relocates fluid II to the central pressure node region and stream I to the sides to form a stable configuration (see Fig. 1)—the process termed as acoustic relocation [27]. The streams, when already in a stable configuration, are prevented from gravitational stratification. When working with fluids where the difference in densities is not too large ( $\hat{\rho} \ll 1$ ), this time-averaged acoustic force density can be expressed as [28]

$$\mathbf{f}_{\text{ac}} = -E_{\text{ac}} \cos(2ky) \nabla \hat{\rho}. \quad (3)$$

Here  $\hat{\rho} = \rho(r, t)/\rho_0 - 1$  is the normalized variation in fluid density for an average initial value  $\rho_0$  and  $\rho(r, t)$  is the local value of density with spatial coordinate  $r$  and time  $t$ . Interestingly, it was observed that in co-flow of fluids having different acoustic impedance, the acoustic streaming vortices are confined close to the channel walls and acoustic streaming is suppressed in the bulk of the fluid. The suppression in acoustic streaming arises from the fluid inhomogeneity-induced acoustic force density  $\mathbf{f}_{\text{ac}}$  which competes with boundary-induced streaming stresses, but the effect diminishes with an increase in flow residence time as the inhomogeneity in acoustic impedance is weakened downstream by diffusion and advection. For example, in the co-flow of a solution of 10% Ficoll PM70 in Milli-Q water and pure Milli-Q water (corresponding to acoustic impedance difference  $\Delta Z \approx 0.8$  MPa s/m), the “size” of the vortex, or the distance of the center of the streaming rolls from the nearest wall ( $d_{\text{inh}}$ ), is shown to be much smaller than that for the corresponding homogeneous flow ( $d_{\text{hom}}$ ) of Milli-Q water,  $d_{\text{inh}}/d_{\text{hom}} \approx 0.2$ , even at a flow residence time of  $\tau_{\text{res}} = 50$  s, indicating considerable suppression of streaming [37,42]. In our study we operate at a similar value of acoustic impedance difference ( $\Delta Z \approx 0.7$  MPa s/m) while the residence times are at least one order of magnitude smaller ( $\tau_{\text{res}} < 5$  s). Therefore, the effects of acoustic streaming can be safely neglected.

### III. EXPERIMENT

#### A. Device fabrication and experimental setup

The microfluidic channel was fabricated on a 4 in. (100) the silicon wafer of 300  $\mu\text{m}$  thickness. The wafer was patterned with a positive photoresist (MICROPOSIT S1813) by exposing to UV lithography. The channels were etched through the entire thickness of the wafer (through-etched) using the DRIE etching technique. The channel has cross-sectional dimensions of 400  $\mu\text{m}$  (W)  $\times$  300  $\mu\text{m}$  (H) throughout and the main channel has a length of  $L = 2$  cm (Fig. 1). The channels were sealed by anodically bonding 500- $\mu\text{m}$ -thick borosilicate glass lids on both the top and bottom by applying a 1000 V voltage bias at a temperature of 450  $^{\circ}\text{C}$ . A piezoceramic transducer (PZT, Sparkler Piezoceramics) with rated resonant frequency 2 MHz was attached to the bottom glass lid using an epoxy adhesive. To enable fluidic access, inlet and outlet holes were drilled into the glass lid on top using CNC micromilling and connected to PTFE tubing. To visualize the flow, an inverted fluorescent microscope (IX71, Olympus) was used in combination with a high-speed CCD camera (SA5, Photron) and a fluorescence attachment. The videos were recorded at a frame rate of 500 frames/s (fps). The fluids were introduced into the channel by connecting the inlet ports to high-performance syringe pumps (neMESYS pump, Cetoni GmbH, Germany).

#### B. Acoustic actuation

Compressional bulk acoustic waves were generated in the silicon channel by applying AC voltage across the PZT transducer attached to the silicon-glass chip. The piezoceramic transducer was actuated with a function generator (SMC100A, Rohde and Schwarz) and the generated sinusoidal signal was amplified with an RF amplifier (75A100A, Amplifier Research) operating in the power range 10–1000 mW. The resonant frequency of the chip was found out by tracking the motion of polystyrene beads (of size 10  $\mu\text{m}$ ) which were continuously introduced into the main channel while the frequency of actuation was varied over the range 1.9–2.1 MHz in steps of 10 kHz. At the resonant frequency of 2.018 MHz, it was seen that the beads experience a strong radiation force and get aligned perfectly along the central pressure nodal plane. The acoustic energy density in the system was computed at different operating voltages using a previously reported technique as follows [11,43,44]. The microbead suspension is initially introduced into the channel while keeping actuation off to ensure the beads are uniformly distributed across the width of the channel. With resonant actuation turned on, the particles which were initially spread out across the width are directed rapidly toward the central pressure node. Tracking the paths of different particles during this motion, the experimental values of particle location ( $y$ ) with time ( $t$ ) are compared with the theoretical expression obtained from balance of the primary radiation force [Eq. (1)] with the Stokes drag force due to viscosity ( $\eta$ ) in the fluid [44]:

$$t = \frac{9\eta}{4\phi(ka)^2 E_{ac}} \ln \left( \frac{\tan [ky(t)]}{\tan [ky(0)]} \right). \quad (4)$$

By fitting the particle location data ( $y, t$ ) from experiments into Eq. (4) with  $E_{ac}$  as fitting parameter, the acoustic energy density in the system can be computed.

#### C. Sample preparation and operating parameters

The fluid samples considered in the study were prepared by adding a density gradient medium iodixanol solution (OptiPrep, Sigma-Aldrich, Bangalore, India) to deionized water (DI) to obtain fluids of different acoustic impedances. Unless otherwise specified, the fluid infused through the central inlet has an iodixanol concentration of  $s = 9\%$  and that through the sides has a higher iodixanol concentration of  $s = 18\%$ . The iodixanol concentration in the fluid infused through center was chosen to ensure that the density of the suspending fluid matches with that of the suspended polystyrene beads,  $\rho_p = 1050 \text{ kg/m}^3$ , ensuring a neutrally buoyant condition. The effect of the particle size was studied by introducing suspensions of monodispersed fluorescent polystyrene

microbeads (microParticles GmbH) of different sizes (of 2, 5, 10, and 15  $\mu\text{m}$  diameter) in different experiments. The total flow rates in the experiments ranged from  $Q_{\text{tot}} = 15 \mu\text{l}/\text{min}$  to  $Q_{\text{tot}} = 200 \mu\text{l}/\text{min}$ , and the acoustic energy densities were varied in the range  $E_{\text{ac}} = 4\text{--}113 \text{ J}/\text{m}^3$ . The flow rate through each side inlet was set to  $Q_{\text{tot}}/4$  while the central inlet flow rate was  $Q_{\text{tot}}/2$ . In experiments devised to compute the relocation timescale, the impedance contrast between the central and side fluids was varied by changing their individual iodixanol concentrations to get  $\Delta s = 9\%$ ,  $18\%$ , and  $27\%$ . A trace quantity of  $0.5\%$  per volume of  $1 \text{ mM}$  Rhodamine-B solution was added to the side fluid and the flow development along the length of the channel was studied by tracking the fluorescent profile.

#### IV. NUMERICAL

To provide a better understanding of the trajectories of particles under the influence of acoustic relocation and radiation force, we develop a simple numerical model where the governing equations are solved in the fluidic domain in the microchannel using finite-element based COMSOL Multiphysics. It suffices to work with a two-dimensional (2D) model as the gradients in iodixanol concentration (or equivalently, local fluid properties) are much smaller along the flow,  $x$  direction as compared to  $y$  and  $z$  directions. A rectangular box of width  $W = 400 \mu\text{m}$  and height  $H = 300 \mu\text{m}$ , matching the experimental cross section formed the 2D computational domain (Fig. 1). The domain is created as three regions of equal width  $W/3$  and fluid properties are defined in the central region and side regions separately. The fluid flow is governed by the incompressible Navier-Stokes equations for Newtonian liquids, which is given as

$$\nabla \cdot (\rho \mathbf{v}) = 0, \quad (5)$$

$$\rho \frac{\partial \mathbf{v}}{\partial t} + \rho (\mathbf{v} \cdot \nabla) \mathbf{v} = \nabla \cdot [-\rho \mathbf{I} + \eta (\nabla \mathbf{v} + (\nabla \mathbf{v})^T)] + \mathbf{f}_b, \quad (6)$$

where  $\eta$  is the viscosity of the fluid,  $\mathbf{f}_b$  is the net volume force (density) acting on the fluid, and  $\mathbf{I}$  is the identity tensor. In our case,  $\mathbf{f}_b = \mathbf{f}_g + \mathbf{f}_{\text{ac}}$  where  $\mathbf{f}_g = -\rho g \mathbf{e}_z$  is the volume force due to gravity and  $\mathbf{f}_{\text{ac}}$  is the time-averaged acoustic force density. The transport of iodixanol (of concentration  $s$ ) is modeled by a general convection-diffusion equation,

$$\frac{\partial s}{\partial t} + \mathbf{v} \cdot \nabla s = \nabla \cdot (D \nabla s), \quad (7)$$

where  $D$  is the diffusion coefficient ( $1 \times 10^{-10} \text{ m}^2/\text{s}$ ) [19]. The fluid properties (viscosity, density, and compressibility) depend on the local iodixanol concentration and are modeled by previously reported relations [19]. No-slip condition for the velocity field ( $\mathbf{v} = 0$ ) and no-flux condition ( $\mathbf{n} \cdot \nabla s = 0$ , where unit vector  $\mathbf{n}$  is the outward surface normal) for the iodixanol concentration field are imposed on all the boundaries of the computational domain. To study the experimentally observed behavior of polystyrene spheres, the particle trajectories are simulated using the in-built particle tracing module. The particles are initially distributed in a uniform pattern in the central third of the channel ( $|y| < W/6$ ). They are modeled as spheres with density corresponding to that of polystyrene and are subjected to drag force due to relocation and primary radiation force. The total force acting on a particle is computed as

$$\mathbf{F}_{\text{total}} = \mathbf{F}_d + \mathbf{F}_{\text{ac}}. \quad (8)$$

The relocation-induced drag force is computed by the Stokes drag relation  $\mathbf{F}_d = 6\pi \eta a \mathbf{v}_{\text{rel}}$  where  $\mathbf{v}_{\text{rel}}$  is the relative velocity of the particle with respect to the fluid. The primary radiation force is directed towards the channel center ( $y = 0$  in the numerical domain) and its magnitude ( $F_{\text{ac}}$ ) is computed using Eq. (1).  $F_{\text{ac}}$  depends on the local value of the acoustic contrast factor ( $\phi$ ) which remains positive but varies with time as the fluid relocation changes local fluid properties. Since the particles are neutrally buoyant in the original medium and we work with low residence times,

the effect of gravity on the particle is not considered. Other effects like interparticle force and particle-fluid interactions are also neglected in the model. The numerical domain is discretized using triangular mesh elements and the convergence analysis is performed by evaluating a metric based on the concentration  $s$  in the central region [45].

## V. RESULTS AND DISCUSSION

In this study we focus only on configurations where the fluid having lower acoustic impedance ( $Z_I$ ) is infused into the channel through the central inlet, and the fluid having higher impedance ( $Z_{II}$ ) enter through the side inlets. This forms an acoustically mismatched configuration ( $\Delta Z = Z_I - Z_{II} < 0$ ) and leads to the relocation of the central fluid stream and the side streams with respect to each other. We first devise a method to compute the time required for the fluids to relocate to stable configuration ( $\tau_{rel}$ ). We then proceed to explore the dynamics of particles under the combined effect of acoustic relocation-induced drag and primary radiation force. Finally, we demonstrate the exchange of HeLa cells and separation HeLa cells from blood cells.

### A. Measuring the time required for acoustic relocation

For a fixed positive impedance difference between the fluid streams ( $\Delta Z$ ) and acoustic energy density  $E_{ac}$ , complete relocation is observed when the time required to transport the fluids to stable configuration, the relocation time ( $\tau_{rel}$ ), is lower than the flow residence time,  $\tau_{res} > \tau_{rel}$ . The flow residence time is defined as  $\tau_{res} = L/u_0$ , where  $L$  is the channel length and  $u_0$  is the average flow velocity at the inlet. The smaller the value of the relocation time, the quicker the relocation proceeds. Here we devise a technique for estimating the value of  $\tau_{rel}$ . As explained in Sec. III C, we add a trace quantity of fluorescent dye Rhodamine-B solution to the higher-impedance side fluid (II) to visualize the relocation process [see Fig. 2(a)]. After the relocation initiates close to the trifurcated inlet junction, the final configuration is obtained at a certain length downstream (denoted here as  $L_{st}$ , the length required to reach stable configuration) beyond which we observe no change in the fluorescent profile, i.e., the width of the fluid stream relocated to the center does not change further with downstream distance indicating completion of relocation. We found that  $L_{st}$  is a function of the impedance difference between the fluids  $\Delta Z$ , acoustic energy density  $E_{ac}$ , and the total flow rate  $Q_{tot}$  [see Fig. 2(a)]. The relocation time can then be computed as the transit time corresponding to  $L_{st}$ , or the time taken by the fluids to travel from the inlet to a downstream distance of  $L_{st}$  given by

$$\tau_{rel} = L_{st}/u_0. \quad (9)$$

The different operating parameters  $Q_{tot}$ ,  $E_{ac}$ , and  $\Delta Z$  were varied over a wide range of values (see Sec. III C) and the relocation time was estimated for each case. To obtain a generalized equation for relocation time, we build on an expression from a previous study as follows. The relocation speed has been analytically expressed by scaling the acoustic force density  $f_{ac}$  and the viscous shear stress at the interface to get [18]

$$u_{ac} \sim \frac{E_{ac} l \hat{\rho}}{\eta_a}, \quad (10)$$

where  $\hat{\rho}$  refers to the normalized density difference between the fluids and  $\eta_a$  refers to the average viscosity of the two fluids. The scaling parameter  $l$  is dependent on the channel dimension in the direction of the standing wave, the mode of actuation, and the orientation of the fluid-fluid interface and thus provides a characteristic relocation length scale for a fixed co-flowing fluid system actuated at half-wave mode. Since the fluids occupy one-third of the channel width at the stable configuration, relocation time  $\tau_{rel}$  can also be expressed based on the relocation speed as

$$\tau_{rel} = \frac{W/3}{u_{ac}}. \quad (11)$$

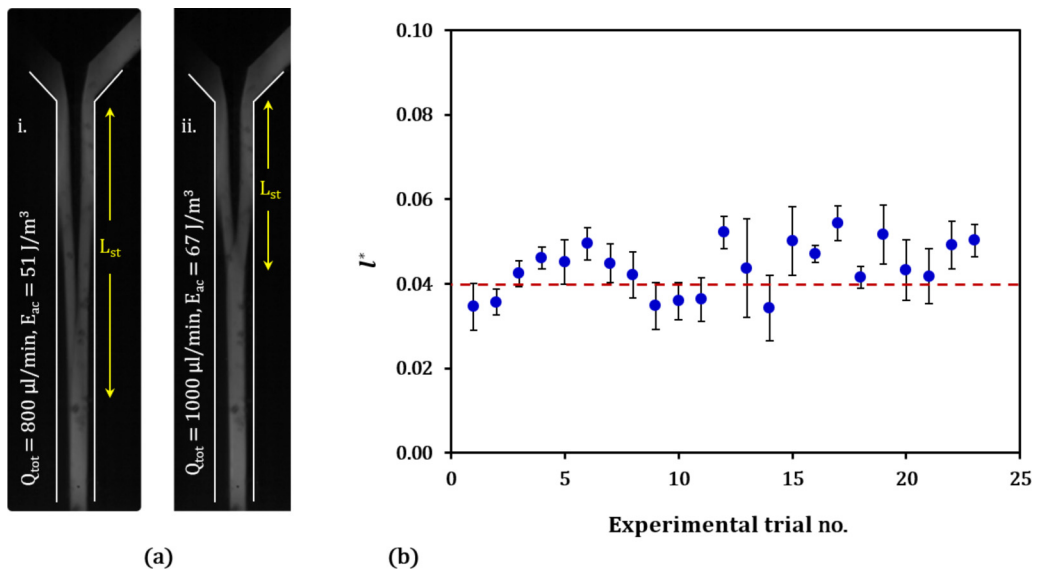


FIG. 2. (a) Experimental images of  $L_{\text{st}}$  at the two different operating conditions: i.  $Q_{\text{tot}} = 800 \mu\text{l}/\text{min}$ ,  $E_{\text{ac}} = 67 \text{ J}/\text{m}^3$ , and difference in acoustic impedance between the fluid streams corresponds to  $\Delta s = 9\%$  difference in iodixanol concentrations, ii.  $Q_{\text{tot}} = 1000 \mu\text{l}/\text{min}$ ,  $E_{\text{ac}} = 67 \text{ J}/\text{m}^3$ , and  $\Delta s = 18\%$ . (b) Relocation length  $l^*$  is predicted from the experimentally measured  $L_{\text{st}}$  from the different trials with different impedance difference  $\Delta Z$ , acoustic energy density  $E_{\text{ac}}$ , and the total flow rate  $Q_{\text{tot}}$  (see Sec. III C). The statistical mean value is based on three different measurements for each set of operating parameters. The average value of the nondimensional length scale  $l^*$  is obtained as  $l^* \approx 0.04 \pm 0.008$ .

The above analytical expression for relocation time is equated to the experimentally obtained value from Eq. (9) to find an estimate for the characteristic length scale  $l$ , or equivalently for  $l^* = l/(W/3)$ , where the relocation length scale  $l$  is nondimensionalized with the width of each fluid stream. From experimentally measured  $L_{\text{st}}$  for different impedance difference  $\Delta Z$ , acoustic energy density  $E_{\text{ac}}$ , and the total flow rate  $Q_{\text{tot}}$ , the relocation length scale  $l^*$  was estimated [see Fig. 2(b)] as  $l^* \approx 0.04 \pm 0.008$ . The relocation length scale predicted herein is generalized for parallel co-flowing fluids and provides a useful estimate for predicting the time taken for complete relocation. However, a high percentage of uncertainty (20%) in the values of  $l^*$  across different trials indicate that the predicted value of  $\tau_{\text{rel}}$  can be used as an order of magnitude estimate rather than an actual value. Therefore, one needs to operate in the regime where the residence time is much larger than the relocation time,  $\tau_{\text{res}} \gg \tau_{\text{rel}}$ , to ensure complete relocation of fluids (rather than just maintaining  $\tau_{\text{res}} > \tau_{\text{rel}}$ ).

## B. Dynamics of a particle under combined relocation-migration

In this section we discuss the particle motion under the combined effect of fluid relocation and acoustophoretic migration due to radiation force. For all cases considered, the particles are initially suspended in the lower impedance fluid (medium I) flowing at the center. As described previously (Sec. III C), monodispersed fluorescent polystyrene particles of different sizes were used in the experiments. We first describe the dynamic effect on a single fluorescent particle of diameter  $a = 15 \mu\text{m}$  before proceeding to generalize the observations based on the relevant flow timescales. The evolution of particle trajectory is obtained by capturing the particle motion with a high-speed camera (at a frame rate of 500 fps) as the particle travels along the length of the channel. The recorded experimental videos were analyzed using Tracker (Open Source Physics), the bright field and fluorescence images were merged for better visualization. In our study, the particles are not

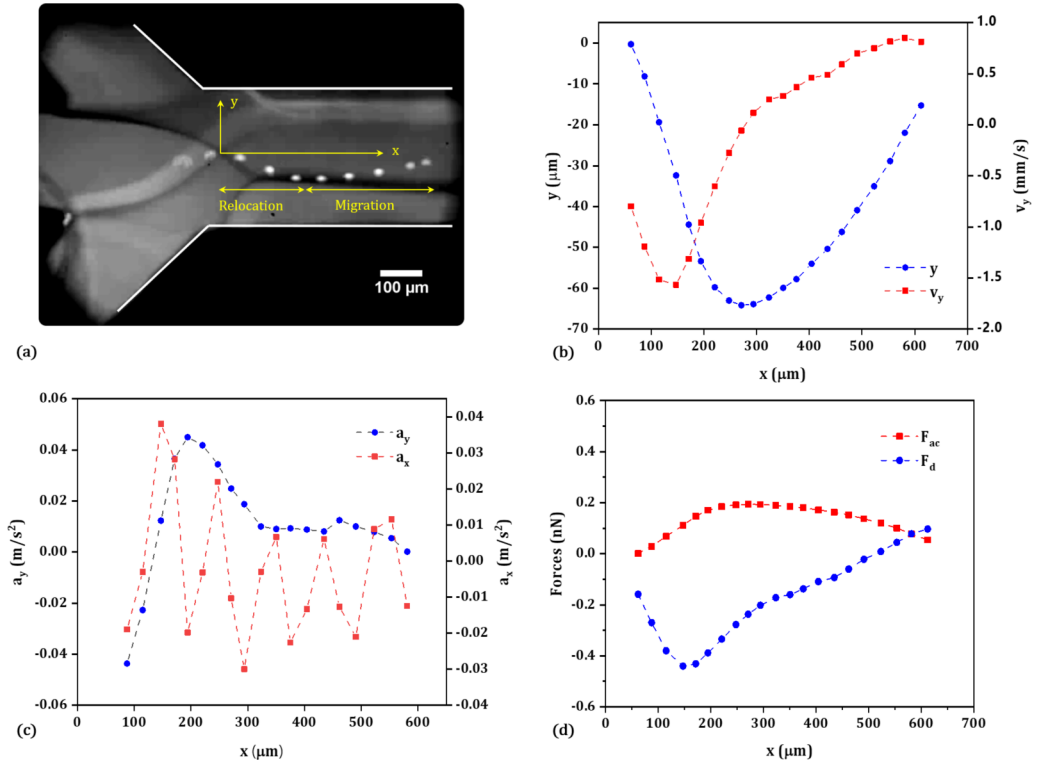


FIG. 3. (a) Experimental image depicting the trajectory of a  $15 \mu\text{m}$  sized particle due to combined relocation and migration, with flow rates  $Q_I = 5 \mu\text{l}/\text{min}$  and  $Q_{II} = 10 \mu\text{l}/\text{min}$ , iodixanol concentration difference  $\Delta s = 9\%$ , acoustic energy density  $E_{ac} = 51 \text{ J}/\text{m}^3$ . As indicated, the dominant force governing the particle motion is initially relocation-induced drag force and downstream, primary radiation force. (b)–(d) Transverse position ( $y$ ) and component of particle velocity ( $v_y$ ), acceleration of the particle in the transverse ( $a_y$ ) and flow directions ( $a_x$ ), relocation-induced drag ( $F_d$ ) and radiation force ( $F_{ac}$ ) acting on the particle, are plotted as functions of downstream distance from the channel inlet ( $x$ ).

hydrodynamically or acoustically prefocused in the central inlet before entering the acoustically active region, and this leads to differences in the starting locations (i.e., lateral positions) of the particles in the main channel. Nonetheless, irrespective of the sizes and starting positions, the particles exhibit some common behavior in terms of their trajectories, and we analyze the motion of a single particle below (further particle trajectories are provided in the Supplemental Material [45]).

Figure 3(a) shows a composite fluorescent and bright-field image depicting the trajectory of a  $15 \mu\text{m}$  diameter particle, with the central fluid stream (of iodixanol concentration  $s = 9\%$ ) flow rate  $Q_I = 5 \mu\text{l}/\text{min}$  and combined flow rate of the fluid stream at the side (of iodixanol concentration  $s = 18\%$ )  $Q_{II} = 10 \mu\text{l}/\text{min}$ . The flow rates were deliberately kept low to enable tracking the full trajectory of a single  $15 \mu\text{m}$  particle within the observation zone. The location of the particle ( $y$ ) and its transverse velocity ( $v_y$ ), as the particle traverses downstream with the flow, are presented in Fig. 3(b). The acceleration of the particle in the flow direction ( $a_x$ ) and the transverse component ( $a_y$ ) are shown in Fig. 3(c). The particle experiences a relocation-induced Stokes drag force ( $F_d$ ) which tends to drive it along with the relocating central fluid to the walls and an opposing acoustophoretic force ( $F_{ac}$ ) towards the central pressure node, which are shown in Fig. 3(d). While the acoustophoretic force acting on the particle is obtained from Eq. (1), the relocation-induced drag force is obtained from experimental trajectory of the particle. To compute the transverse component

of relocation-induced drag force, the relative velocity of the particle  $v_y$  is measured from particle location data  $(y, t)$  and the lateral drag force acting on the particle is computed as  $F_d = 6\pi\eta av_y$ .

From Fig. 3(d) it can be observed that initially the relocation-induced drag  $F_d$  dominates over  $F_{ac}$  and hence the particle is dragged towards the side walls. At an acoustic energy density of  $E_{ac} = 51 \text{ J/m}^3$ , the  $15 \text{ }\mu\text{m}$  sized particle traverses a maximum lateral distance of  $y \approx 60 \text{ }\mu\text{m}$  before being driven back to the pressure node by the radiation force. From the experimental image, it is clear that the relocation-induced drag force only acts for a distance up to  $L_{st} = 0.3 \text{ mm}$ , beyond which the trajectory is fully defined by  $F_{ac}$ . For suspensions involving smaller particles ( $a \leq 2 \text{ }\mu\text{m}$ ), the drag force leads to complete carry-over of particles along with the relocating fluid to the side third of the channel (i.e.,  $|y| > W/6$ ). Since the drag force and the radiation force scale as  $F_d \sim a$  and  $F_{ac} \sim a^3$ , respectively, smaller particles remain in the original relocated fluid at the outlet even at the lowest flow rate of  $Q_{tot} = 15 \text{ }\mu\text{l/min}$  used in our study.

Generally, the inertia of the particle is neglected since the timescale for the acceleration of the particle,  $\tau_a = 2a^2\rho/9\eta \sim 42 \text{ }\mu\text{s}$ , is small [46] compared to the time for translation ( $\tau \sim 0.2 \text{ s}$ ). Nonetheless, the experimentally computed particle acceleration ( $a = dv/dt$ ) revealed interesting results. We observe that the acceleration of the particle in the flow direction ( $a_x$ ) depicts an oscillating behavior while the transverse component ( $a_y$ ) changes from an initially large negative value to a positive value downstream as the fluids attain a stable configuration after relocation [Fig. 3(c)]. Further downstream, the value of acceleration reduces and goes to zero as the particle attains the equilibrium position close to the center of the channel. The oscillating behavior of the component of acceleration along flow  $a_x$  can be attributed to multiple reasons. As the particle undergoes acoustic relocation, the location of the particle in the  $y$  and  $z$  directions changes leading to a rapid variation in the axial velocity along  $e_x$  due to the 3D nature of the axial velocity profile. Also, the component of Stokes drag force on the particle in the flow direction is dependent on the local fluid viscosity which varies as the particle traverses laterally between the fluids and could also cause such oscillations. Another possible reason for the occurrence of this variation in  $a_x$  could be the presence of weak resonances in the flow direction, attributed to a variation in the axial radiation force [47].

### C. Different regimes of medium exchange and comparison of timescales

When a dilute suspension of monodispersed particles is introduced through the central inlet, the combined effect of acoustic relocation and radiation force can result in (a) complete medium exchange wherein the particles dragged along with the relocating carrier medium are driven back to the nodal region at the channel center and enter the new target medium; (b) partial medium exchange wherein the radiation force is insufficient to drive all the particles to the central target medium and are thus the particles are present in both the media; or (c) no medium exchange, where the particles relocate along with and remain in the original carrier medium. For a suspension of  $2 \text{ }\mu\text{m}$  sized fluorescent particles in a carrier medium ( $s = 9\%$  iodixanol) injected through the central inlet at  $40 \text{ }\mu\text{l/min}$  and higher acoustic impedance fluid ( $s = 18\%$  iodixanol), or target medium injected at  $20 \text{ }\mu\text{l/min}$  through each side inlet, depending on the acoustic energy density, the three different regimes are delineated in Fig. 4(a).

Exchange of the suspending media is characterized using the fluorescent intensity profile (that is proportional to the particle concentration) close to the outlet of the main channel, as shown in Fig. 4(b). We observe a complete medium exchange when  $E_{ac} = 113 \text{ J/m}^3$  [Fig. 4(a) iv], the normalized fluorescent intensity in the sides (i.e.,  $|y| > W/6$ ), remains below 0.1 indicating that all the particles are transferred to the target medium at the center [Fig. 4(b) iii]. Similarly, no medium exchange regime is observed at  $E_{ac} = 31 \text{ J/m}^3$  [Fig. 4(a) ii], the fluorescent intensity in the channel center (i.e.,  $|y| < W/6$ ) is below 0.1 indicating that the particles remain in the relocated original carrier medium at the sides [Fig. 4(b) i]. In the range  $31 < E_{ac} < 113 \text{ J/m}^3$  [Fig. 4(a) iii], the fluorescent intensity in both the fluid streams is above 0.1 indicating a partial medium exchange where the particles are distributed in both the carrier and target media [Fig. 4(b) ii].

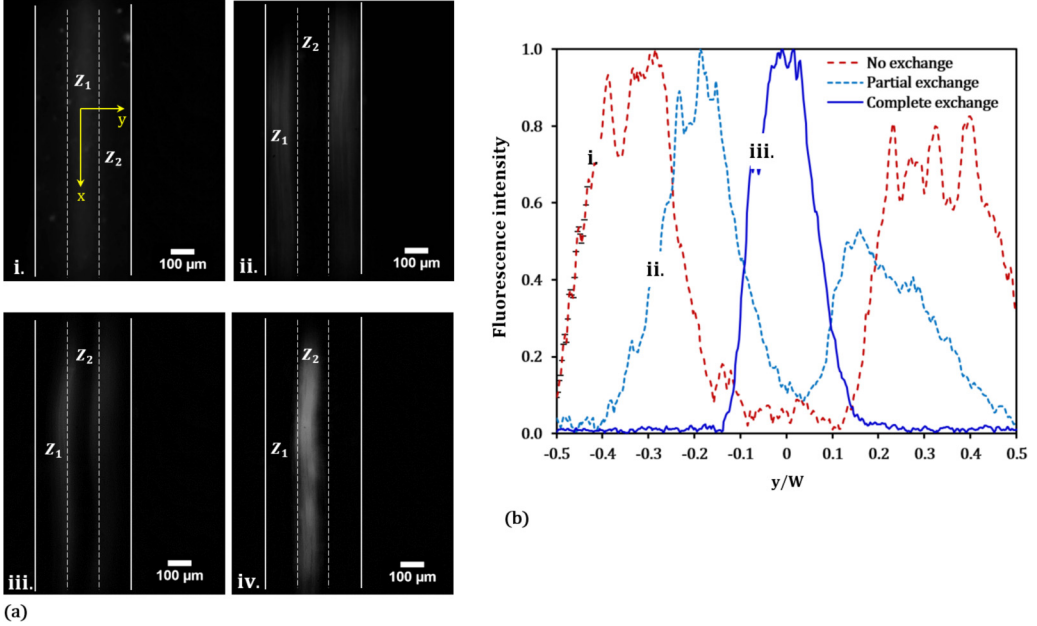


FIG. 4. (a) The initial configuration close to the inlet (i) and the three regimes close to the outlet are shown at: ii.  $E_{ac} = 31 \text{ J/m}^3$ , zero medium exchange where the particles remain in the original carrier medium; iii.  $E_{ac} = 67 \text{ J/m}^3$ , partial exchange where the particles are present in both the media; and iv.  $E_{ac} = 113 \text{ J/m}^3$ , a full exchange where the particles are in the target medium. The dotted lines indicate the central third of the channel width. (b) The fluorescent intensity profile across the width of the channel also delineate the three different medium exchange regimes.

The final configuration of the system is a function of the two competing forces:  $F_{ac}$  and  $F_d$ , and the flow residence time in the channel. The relocation-migration behavior of the particles is generalized in terms of a phase diagram encompassing variations in the relevant parameters, i.e., particle size ( $a$ ), the acoustic energy density ( $E_{ac}$ ), and total flow rate ( $Q_{tot}$ ), as depicted in Fig. 5. The behavior is characterized by using two dimensionless parameters ( $\psi$  and  $\xi$ ) which relate to the three important timescales: residence timescale ( $\tau_{res} = L/u_0$ ), radiation force timescale ( $\tau_{ac} = 3\eta u_0/2\phi a^2 k E_{ac}$ ), and the relocation timescale [ $\tau_{rel} = \eta(W/3)/(E_{ac}l\hat{\rho})$ ] as follow:

$$\psi = \frac{\tau_{res}}{\tau_{rel}} = \frac{L}{u_0} \frac{E_{ac}l\hat{\rho}}{\eta(W/3)}; \quad \xi = \frac{\tau_{res}}{\tau_{ac}} = \frac{L}{u_0} \frac{2\phi a^2 k E_{ac}}{3\eta u_0}. \quad (12)$$

Please note that a smaller timescale indicates a stronger force. We characterize the three distinct regimes: no medium exchange, partial medium exchange, and complete medium exchange regimes, in the phase diagram. For  $\xi < 0.3$  where  $\tau_{ac} \gg \tau_{res}$ , we observed zero medium exchange, i.e., the particles are dragged to the side along with the original suspending fluid (medium I) and do not enter the central fluid (medium II). It is observed that the “no medium exchange” regime is independent of  $\psi$ , which is primarily because in addition to operating in range of values to ensure complete relocation ( $\tau_{rel} \ll \tau_{res}$ ), the radiation force timescale is also much larger than the relocation time ( $\xi = \tau_{res}/\tau_{ac} < 1$  leads to  $\tau_{rel} \ll \tau_{ac}$ ), so the timescales of the two influences on particle trajectory, relocation and radiation force, can be separated. When the flow is operated in this regime, relocation to stable configuration is completed very close to the trifurcated junction at the main channel. It is therefore similar to a configuration where the suspension is infused through the side inlets with the higher acoustic impedance fluid infused through the center.

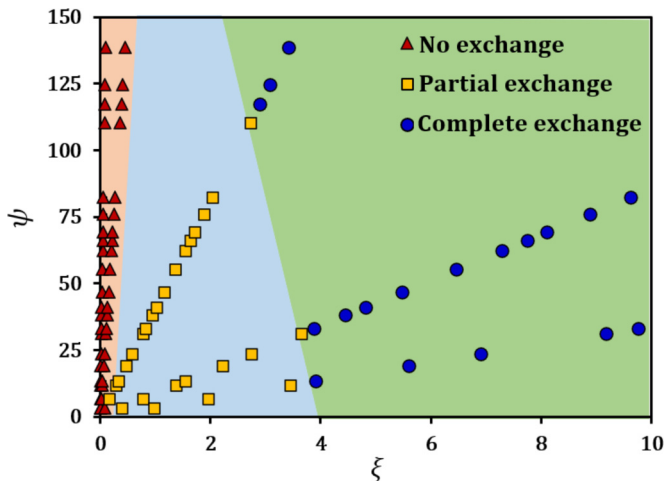


FIG. 5. A general phase diagram encompassing variations in the relevant parameters: particle size ( $a$ ), the acoustic energy density ( $E_{ac}$ ), and total flow rate ( $Q_{tot}$ ), to represent the three different regimes, complete exchange, partial exchange, and no exchange of medium, in terms of the two dimensionless parameters  $\psi = \tau_{res}/\tau_{rel}$  and  $\xi = \tau_{res}/\tau_{ac}$ .

For a given  $\psi$ , the complete medium exchange is possible when  $\xi > 4$ , i.e.,  $\tau_{res} \gg \tau_{ac}$ , so the particles that are initially dragged along with the relocating original medium (I) have sufficient transit time in the channel to enter the target medium (II). In an intermediate range of  $\xi$  we observe that the  $\tau_{res}$  is not large enough for all the particles to migrate back to the center (II), and therefore only a partial exchange of media is attained. Here we observe that for  $0.3 < \xi < 4$ , depending on how quickly the relocation is completed, i.e., the value of  $\psi$ , the particles may reenter the central fluid stream fully or partially. We also observe that the critical  $\xi$  above which complete medium exchange is possible decreases with an increase in the value of  $\psi$ , i.e., as the time to complete relocation reduces, the particle motion is controlled purely by radiation force  $F_{ac}$  over a larger channel length. For the cases wherein the relocation time is higher than the residence time ( $\tau_{rel} > \tau_{res}$ ), the relocation will be incomplete and are hence not investigated in the present study as they may not have any practical applications.

#### D. Numerical results

In the numerical model we show results for parameter values (iodixanol concentration  $s = 9\%$ ,  $18\%$  and acoustic energy density  $E_{ac} = 51 \text{ J/m}^3$ ) corresponding to experimental conditions described in Fig. 3. Since the system has inherent symmetry (central high impedance fluid flanked on either side by similar low impedance fluid), it suffices to show results for only half the domain ( $y > 0$ ). In Fig. 6 the results are shown at four different time instants from  $\tau = 0 \text{ s}$  to  $\tau = 0.30 \text{ s}$ . Since the numerical model solves for hydrodynamic effects in the channel cross section, the time variable in the model corresponds to the transit time from the inlet,  $\tau = x/u_0$ . For example, for modeling a flow with residence time  $\tau_{res} = 0.30 \text{ s}$ , it suffices to simulate from  $\tau = 0 \text{ s}$  (fluid configuration at the channel inlet) up to  $\tau = 0.30 \text{ s}$  (fluid configuration at the channel outlet). In Fig. 6(a) the bulk relocation of the fluids is shown through profiles of iodixanol concentration where starting from an initial impedance mismatch (corresponding to  $\Delta s = 9\%$ ), the acoustic force density  $f_{ac}$  acts to transport the higher iodixanol concentration side fluid to the center while the central fluid gets transported to the sides to form stable configuration at  $\tau = 0.30 \text{ s}$ .

The numerically computed trajectories of  $10$  and  $2 \mu\text{m}$  sized particles is shown in Fig. 6(b). At time  $\tau = 0 \text{ s}$ , particles of both sizes are released uniformly in the central fluid. As the relocation

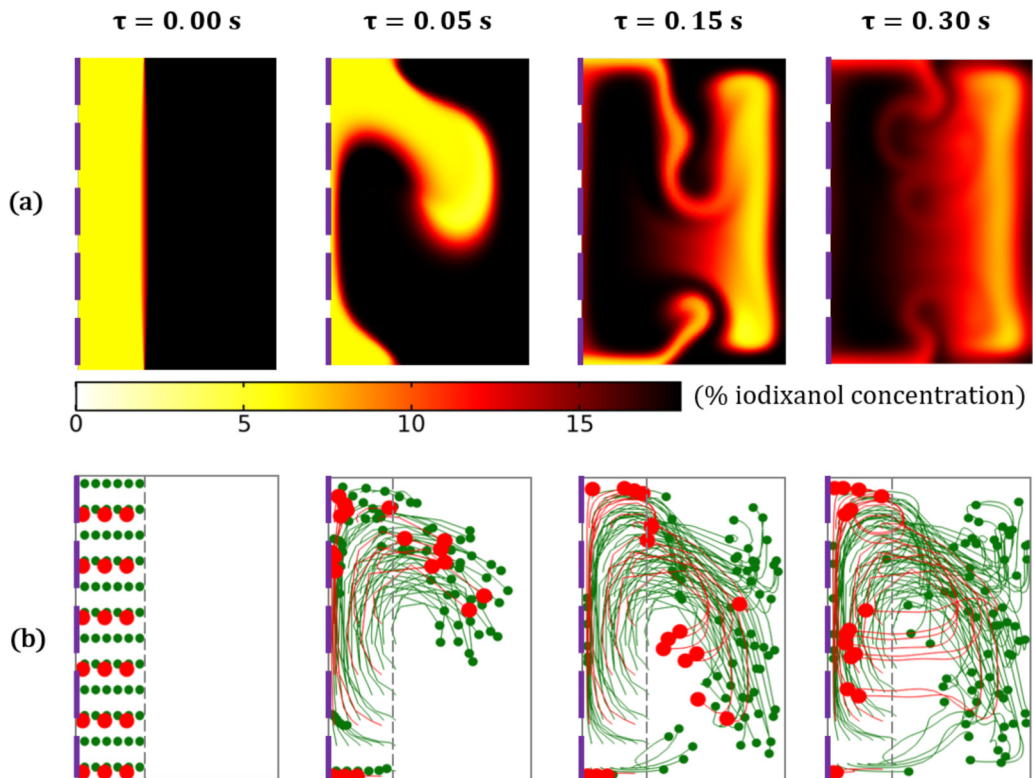


FIG. 6. (a) The bulk relocation of the fluids owing to an acoustic impedance difference between the fluids with  $s = 18\%$  iodixanol at the sides and  $s = 9\%$  iodixanol at the center is shown at various stages of development. (b) The trajectories of particles of size  $10$  (red circles) and  $2 \mu\text{m}$  (green circles) due to combined relocation and migration shows that only the larger particles have entered the central fluid after relocation. Only half of the domain is shown due to symmetry about  $y = 0$  (marked by purple lines).

initiates, the particles are dragged along with the relocating central fluid. The smaller  $2 \mu\text{m}$  sized particles travel farther away from the channel centerline as compared to the larger  $10 \mu\text{m}$  sized particles due to lower radiation force. At  $\tau = 0.30$  s, it is observed that the  $10 \mu\text{m}$  sized particles have entered the relocated higher impedance fluid (target medium) at the center, while the  $2 \mu\text{m}$  sized particles are retained by the original medium at the walls. In the simulation results, for  $10 \mu\text{m}$  particles that exhibit complete exchange, the values of  $\psi = 38$  and  $\xi = 4.44$  and for the  $2 \mu\text{m}$  particle that exhibits no medium exchange, the values of  $\psi = 38$  and  $\xi = 0.2$ , are in agreement with the experimental data for the complete exchange and no exchange regimes presented in Fig. 5. The numerical model can therefore be used to accurately predict the final medium exchange configuration at different operating conditions.

#### E. Demonstration of medium exchange of HeLa cells and separation of HeLa cells from blood cells

By using a total flow rate of  $Q_{\text{I}} = 30 \mu\text{l}/\text{min}$  and  $Q_{\text{II}} = 40 \mu\text{l}/\text{min}$  and energy density of  $31 \text{ J}/\text{m}^3$ , we demonstrated the transfer of circulating tumor cells, HeLa cells (size  $\sim 16 \mu\text{m}$ ) [48] suspended in the low impedance fluid (medium I, PBS) initially located at the center to the high impedance fluid (medium II, PBS with  $s = 9\%$  iodixanol) that finally relocates to the center, as shown in Fig. 7(a). The experimental conditions correspond to  $\psi = 82.3$  and  $\xi = 24.8$ , which fall in the complete exchange regime as per the phase diagram (Fig. 5). The HeLa cells introduced into

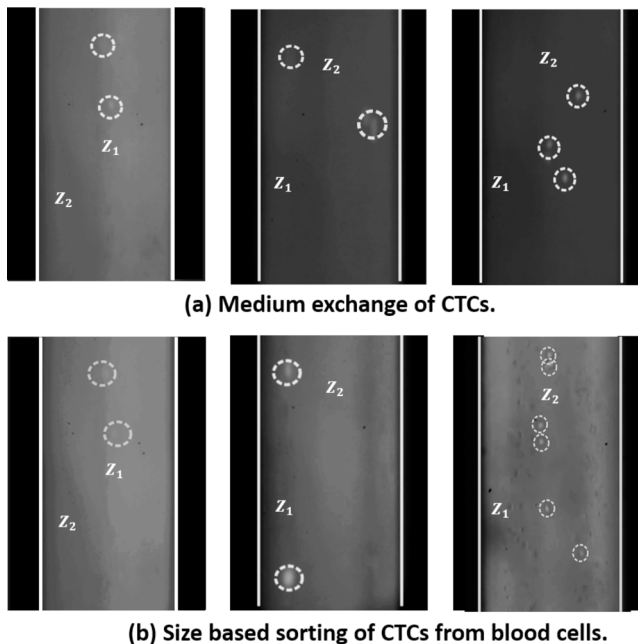


FIG. 7. (a) Medium exchange of HeLa cells from a low impedance fluid (medium I, PBS) initially located at the center to a high impedance fluid (medium II, PBS with 9% iodixanol), a total flow rate of  $70 \mu\text{l}/\text{min}$ , and energy density of  $E_{ac} = 67 \text{ J}/\text{m}^3$ . (b) Size-based separation of HeLa cells from the blood cells using the combined relocation-migration technique, at a total flow rate of  $70 \mu\text{l}/\text{min}$  and  $E_{ac} = 67 \text{ J}/\text{m}^3$ .

the channel in the low acoustic impedance fluid at the inlet and collected at the outlet of the high impedance fluid were enumerated using a hemocytometer, and a medium exchange efficiency of  $98 \pm 1.2\%$  was found. Furthermore, by making use of the observation that smaller particles exhibit no exchange and larger particles exhibit complete exchange under similar operating conditions, we demonstrate separation of HeLa cells ( $\sim 16 \mu\text{m}$ ) from the blood cells ( $\sim 5\text{--}10 \mu\text{m}$ ) [see Fig. 7(b)]. HeLa cells were spiked in diluted blood suspension (whole blood diluted  $\times 100$  in PBS) with a concentration of  $10^6$  HeLa cells/ml and infused as the central fluid (medium I). A higher acoustic impedance fluid (PBS with  $s = 9\%$  iodixanol) was infused at the sides (medium II). At a total flow rate of  $70 \mu\text{l}/\text{min}$  and  $E_{ac} = 67 \text{ J}/\text{m}^3$ , we observed that after the initial relocation-induced drag drives both HeLa cells and blood cells to the sides, the larger HeLa cells migrate back much closer to the pressure node as compared to RBCs. With these operating conditions, we obtained an average separation efficiency of  $96 \pm 0.6\%$  and purity of  $93 \pm 1.6\%$ . On using less diluted blood (higher RBC concentrations), the recovery of HeLa cells is still high but the separation efficiency is seen to be significantly lower. At higher RBC concentrations, the cells are hydrodynamically coupled and this results in the advection of the suspending fluid as the cells migrate towards the center. In addition, the non-negligible secondary acoustic radiation force leads to the formation of clumps of concentrated cells which also hinders separation. So our technique can be used for handling HeLa cells at a concentration of  $10^6$  cells/ml in diluted whole blood (diluted  $\times 100$ ) while offering excellent separation efficiency and purity.

## VI. CONCLUSION

We studied the transfer of particles between co-flowing fluids in a microchannel exposed to standing bulk acoustic waves due to the combined effect of acoustic relocation-induced drag and primary radiation force. We found that upon acoustic actuation, the particles initially suspended in

a low impedance medium at the channel center (nodal plane) are first driven toward the side walls (antinodal plane) along with the relocating medium and then migrate into the high impedance target medium that relocates to the center from the sides. The behavior of the particles under the combined effect was explained using the Stokes drag force due to relocation and the primary radiation force. The relocation and migration dynamics of the particles was generalized in terms of the ratios of the relevant timescales, i.e., the ratio of the residence to relocation timescale ( $\psi = \tau_{\text{res}}/\tau_{\text{rel}}$ ) and residence to acoustic timescale ( $\xi = \tau_{\text{res}}/\tau_{\text{ac}}$ ). For inhomogeneous co-flow of fluids used in our studies having different impedance difference  $\Delta Z$ , acoustic energy density  $E_{\text{ac}}$ , and total flow rate  $Q_{\text{tot}}$ , we estimated a dimensionless relocation length scale ( $l^* \approx 0.04$ ) that enables the estimation of the relocation timescale. Experimentally we unraveled that depending on the operating parameters, particle size, flow rates, and energy density, three different regimes are possible—complete medium exchange, partial medium exchange, and no medium exchange, which were represented in a phase diagram in terms of  $\psi$  and  $\xi$ . We found that complete medium exchange is observed for  $\xi > 4$  with  $\psi < 25$  and the critical  $\xi$  for complete medium exchange decreases with increase in the value of  $\psi$ , no medium exchange is observed for  $\xi < 0.3$ , independent of  $\psi$ , partial medium exchange for  $0.3 < \xi < 4$ , depending on  $\psi$ . Numerical simulations were used to predict the complete migration of larger  $10 \mu\text{m}$  sized particles to the target medium and nonmigration of smaller  $2 \mu\text{m}$  sized particles, in agreement with the experimental observations, which also suggested that the technique can be used for size-based particle/cell sorting. Medium exchange of biological cells and size-based separation of cells were demonstrated which showed the potential application of the study in biochemical assays.

#### ACKNOWLEDGMENTS

A.K.S. thanks DST for providing the financial support for the Swarnajayanti Fellowship project via Grant No. DST/SJF/ETA-03/2017-18. A.K.S. acknowledges research funding from the MHRD, Government of India through the Institute of Eminence (IoE) scheme via Grant No. 11/9/2019-U.3(A). The support of CNNP, IIT Madras for the device fabrication is appreciated.

- 
- [1] F. Petersson, L. Åberg, A. M. Swärd-Nilsson, and T. Laurell, Free flow acoustophoresis: Microfluidic-based mode of particle and cell separation, *Anal. Chem.* **79**, 5117 (2007).
  - [2] T. Laurell, F. Petersson, and A. Nilsson, Chip integrated strategies for acoustic separation and manipulation of cells and particles, *Chem. Soc. Rev.* **36**, 492 (2007).
  - [3] X. Ding, S.-C. S. Lin, B. Kiraly, H. Yue, S. Li, I.-K. Chiang, J. Shi, S. J. Benkovic, and T. J. Huang, On-chip manipulation of single microparticles, cells, and organisms using surface acoustic waves, *Proc. Natl. Acad. Sci. USA* **109**, 11105 (2012).
  - [4] L. Schmid, D. A. Weitz, and T. Franke, Sorting drops and cells with acoustics: Acoustic microfluidic fluorescence-activated cell sorter, *Lab Chip* **14**, 3710 (2014).
  - [5] C. Grenvall, C. Magnusson, H. Lilja, and T. Laurell, Concurrent isolation of lymphocytes and granulocytes using prefocused free flow acoustophoresis, *Anal. Chem.* **87**, 5596 (2015).
  - [6] Y. Chen, M. Wu, L. Ren, J. Liu, P. H. Whitley, L. Wang, and T. J. Huang, High-throughput acoustic separation of platelets from whole blood, *Lab Chip* **16**, 3466 (2016).
  - [7] M. Antfolk, P. B. Muller, P. Augustsson, H. Bruus, and T. Laurell, Focusing of sub-micrometer particles and bacteria enabled by two-dimensional acoustophoresis, *Lab Chip* **14**, 2791 (2014).
  - [8] P. Dow, K. Kotz, S. Gruszka, J. Holder, and J. Fiering, Acoustic separation in plastic microfluidics for rapid detection of bacteria in blood using engineered bacteriophage, *Lab Chip* **18**, 923 (2018).
  - [9] P. Ohlsson, M. Evander, K. Petersson, L. Mellhammar, A. Lehmusvuori, U. Karhunen, M. Soikkeli, T. Seppä, E. Tuunainen, A. Spangar, P. Von Lode, K. Rantakokko-Jalava, G. Otto, S. Scheduling, T. Soukka, S. Wittfooth, and T. Laurell, Integrated acoustic separation, enrichment, and microchip polymerase chain reaction detection of bacteria from blood for rapid sepsis diagnostics, *Anal. Chem.* **88**, 9403 (2016).

- [10] S. Karthick, P. N. Pradeep, P. Kanchana, and A. K. Sen, Acoustic impedance-based size-independent isolation of circulating tumour cells from blood using acoustophoresis, *Lab Chip* **18**, 3802 (2018).
- [11] S. Karthick and A. K. Sen, Improved understanding of the acoustophoretic focusing of dense suspensions in a microchannel, *Phys. Rev. E* **96**, 052606 (2017).
- [12] A. Nath and A. K. Sen, Acoustic Behavior of a Dense Suspension in an Inhomogeneous Flow in a Microchannel, *Phys. Rev. Appl.* **12**, 054009 (2019).
- [13] O. Jakobsson, S. S. Oh, M. Antfolk, M. Eisenstein, T. Laurell, and H. T. Soh, Thousand-fold volumetric concentration of live cells with a recirculating acoustofluidic device, *Anal. Chem.* **87**, 8497 (2015).
- [14] M. Antfolk, C. Magnusson, P. Augustsson, H. Lilja, and T. Laurell, Acoustofluidic, label-free separation and simultaneous concentration of rare tumor cells from white blood cells, *Anal. Chem.* **87**, 9322 (2015).
- [15] M. Evander and J. Nilsson, Acoustofluidics 20: Applications in acoustic trapping, *Lab Chip* **12**, 4667 (2012).
- [16] B. Hammarström, T. Laurell, and J. Nilsson, Seed particle-enabled acoustic trapping of bacteria and nanoparticles in continuous flow systems, *Lab Chip* **12**, 4296 (2012).
- [17] I. Leibacher, P. Reichert, and J. Dual, Microfluidic droplet handling by bulk acoustic wave (BAW) acoustophoresis, *Lab Chip* **15**, 2896 (2015).
- [18] J. T. Karlsen and H. Bruus, Acoustic Tweezing and Patterning of Concentration Fields in Microfluidics, *Phys. Rev. Appl.* **7**, 034017 (2017).
- [19] P. Augustsson, J. T. Karlsen, H.-W. Su, H. Bruus, and J. Voldman, Iso-acoustic focusing of cells for size-insensitive acousto-mechanical phenotyping, *Nat. Commun.* **7**, 11556 (2016).
- [20] D. Hartono, Y. Liu, P. L. Tan, X. Y. S. Then, L.-Y. L. Yung, and K.-M. Lim, On-chip measurements of cell compressibility via acoustic radiation, *Lab Chip* **11**, 4072 (2011).
- [21] L. V. King, On the acoustic radiation pressure on spheres, *Proc. R. Soc. London Ser. A* **147**, 212 (1934).
- [22] K. Yosioka and Y. Kawasima, Acoustic radiation pressure on a compressible sphere, *Acta Acust. United Acust.* **5**, 167 (1955).
- [23] G. T. Silva and H. Bruus, Acoustic interaction forces between small particles in an ideal fluid, *Phys. Rev. E* **90**, 063007 (2014).
- [24] S. Z. Hoque and A. K. Sen, Interparticle acoustic radiation force between a pair of spherical particles in a liquid exposed to a standing bulk acoustic wave, *Phys. Fluids* **32**, 072004 (2020).
- [25] S. M. Woodside, B. D. Bowen, and J. M. Piret, Measurement of ultrasonic forces for particle-liquid separations, *AIChE J.* **43**, 1727 (1997).
- [26] M. Settnes and H. Bruus, Forces acting on a small particle in an acoustical field in a viscous fluid, *Phys. Rev. E* **85**, 016327 (2012).
- [27] S. Deshmukh, Z. Brzozka, T. Laurell, and P. Augustsson, Acoustic radiation forces at liquid interfaces impact the performance of acoustophoresis, *Lab Chip* **14**, 3394 (2014).
- [28] J. T. Karlsen, P. Augustsson, and H. Bruus, Acoustic Force Density Acting on Inhomogeneous Fluids in Acoustic Fields, *Phys. Rev. Lett.* **117**, 114504 (2016).
- [29] E. Hemachandran, T. Laurell, and A. K. Sen, Continuous Droplet Coalescence in a Microchannel Coflow Using Bulk Acoustic Waves, *Phys. Rev. Appl.* **12**, 044008 (2019).
- [30] E. Hemachandran, S. Karthick, T. Laurell, and A. K. Sen, Relocation of coflowing immiscible liquids under acoustic field in a microchannel, *Europhys. Lett.* **125**, 54002 (2019).
- [31] G. P. Gautam, R. Gurung, F. A. Fencel, and M. E. Piyasena, Separation of sub-micron particles from micron particles using acoustic fluid relocation combined with acoustophoresis, *Anal. Bioanal. Chem.* **410**, 6561 (2018).
- [32] J. J. Hawkes, R. W. Barber, D. R. Emerson, and W. T. Coakley, Continuous cell washing and mixing driven by an ultrasound standing wave within a microfluidic channel, *Lab Chip* **4**, 446 (2004).
- [33] M. Wu, A. Ozcelik, J. Rufo, Z. Wang, R. Fang, and T. Jun Huang, Acoustofluidic separation of cells and particles, *Microsyst. Nanoeng.* **5**, 32 (2019).
- [34] P. Augustsson, L. B. Åberg, A. M. K. Swärd-Nilsson, and T. Laurell, Buffer medium exchange in continuous cell and particle streams using ultrasonic standing wave focusing, *Microchim. Acta* **164**, 269 (2009).

- [35] A. Lenshof, C. Magnusson, and T. Laurell, Acoustofluidics 8: Applications of acoustophoresis in continuous flow microsystems, *Lab Chip* **12**, 1210 (2012).
- [36] P. Augustsson, J. Persson, S. Ekström, M. Ohlin, and T. Laurell, Decomplexing biofluids using microchip based acoustophoresis, *Lab Chip* **9**, 810 (2009).
- [37] J. T. Karlsen, W. Qiu, P. Augustsson, and H. Bruus, Acoustic Streaming and its Suppression in Inhomogeneous Fluids, *Phys. Rev. Lett.* **120**, 054501 (2018).
- [38] F. Petersson, A. Nilsson, H. Jönsson, and T. Laurell, Carrier medium exchange through ultrasonic particle switching in microfluidic channels, *Anal. Chem.* **77**, 1216 (2005).
- [39] H. Bruus, Acoustofluidics 7: The acoustic radiation force on small particles, *Lab Chip* **12**, 1014 (2012).
- [40] F. Nadal and E. Lauga, Small acoustically forced symmetric bodies in viscous fluids, *J. Acoust. Soc. Am.* **139**, 1081 (2016).
- [41] A. A. Doinikov, Acoustic radiation pressure on a rigid sphere in a viscous fluid, *Proc. R. Soc. London Ser. A* **447**, 447 (1994).
- [42] W. Qiu, J. T. Karlsen, H. Bruus, and P. Augustsson, Experimental Characterization of Acoustic Streaming in Gradients of Density and Compressibility, *Phys. Rev. Appl.* **11**, 024018 (2019).
- [43] S. Karthick and A. Sen, Role of Shear Induced Diffusion in Acoustophoretic Focusing of Dense Suspensions, *Appl. Phys. Lett.* **109**, 014101 (2016).
- [44] R. Barnkob, P. Augustsson, T. Laurell, and H. Bruus, Measuring the local pressure amplitude in microchannel acoustophoresis, *Lab Chip* **10**, 563 (2010).
- [45] See Supplemental Material at <http://link.aps.org/supplemental/10.1103/PhysRevFluids.6.044201> for more details on the mesh convergence study and different experimentally obtained trajectories of particles.
- [46] P. B. Muller, R. Barnkob, M. J. H. Jensen, and H. Bruus, A numerical study of microparticle acoustophoresis driven by acoustic radiation forces and streaming-induced drag forces, *Lab Chip* **12**, 4617 (2012).
- [47] P. Augustsson, R. Barnkob, S. T. Wereley, H. Bruus, and T. Laurell, Automated and temperature-controlled micro-PIV measurements enabling long-term-stable microchannel acoustophoresis characterization, *Lab Chip* **11**, 4152 (2011).
- [48] P. Li, Z. Mao, Z. Peng, L. Zhou, Y. Chen, P.-H. Huang, C. I. Truica, J. J. Drabick, W. S. El-Deiry, M. Dao, S. Suresh, and T. J. Huang, Acoustic separation of circulating tumor cells, *Proc. Natl. Acad. Sci. USA* **112**, 4970 (2015).